NOVEL METHOD OF NONINVASIVE DETECTION AND ASSESSMENT OF GAS EMBOLI AND DCS

Dr. Kirill V Larin (P.I.)

Department of Biomedical Engineering, University of Houston

Email: klarin@uh.edu, Ph: 8328428834

Abstract

Noninvasive functional imaging, monitoring and quantification of microbubbles forming in blood and tissues upon rapid changes in barometric pressure are extremely important for effective therapy and diagnostics of several diseases as well as for imaging and drug delivery projects. However, current techniques are unable of imaging and efficient detection of bubbles with diameter less than 50 micrometers. The goal of this proposal was to develop novel Phase-Sensitive Swept Source Optical Coherence Tomography (PhS-SSOCT) technique capable of real-time, sensitive, accurate, and noninvasive imaging, monitoring, and quantification of microbubbles in tissues. During these studies, a novel phase resolved system based on Swept Source Optical Coherence Tomography (SSOCT) has been developed. The system has an axial resolution of 10 μm, phase sensitivity of 0.03 radians, imaging depth of up to 6 mm in air, and in-depth scanning speed of 20 kHz for a single A-line. The performance of the sensing system was carefully evaluated in optical phantoms containing gas microbubbles with different diameter. Obtained results demonstrate that bubbles with diameter greater than 10 μm could be detected by both structural imaging and phase response whereas bubbles with diameters less than 10 μm could be detected by the phase response of the SSOCT with high sensitivity. The accuracy for measurement of the diameter of gas microbubbles is limited to 10 μm in structural imaging and 0.01 μm in phase-sensitive monitoring. Preliminary studies were also performed in animals *in vivo* for the rapid assessment of the circulating microbubbles. The *in vivo* results demonstrate capability of the developed instrument to image bubbles with diameter above 8 μm. The results from the study indicate that the developed SSOCT system could be used to detect fast-moving microbubbles and warrant further investigation in biological tissues *in vivo*.

Acknowledgements

The study is supported by a grant from Office of Naval Research Young Investigator Program, Undersea Medicine Research Program (Code: 34; PO: CDR Matthew Swiergosz).

Report Documentation Page

Form Approved
OMB No. 0704-0188

1. REPORT DATE	2. REPORT TYPE	3. DATES COVERED
DEC 2010	**N/A**	**-**

4. TITLE AND SUBTITLE
Novel Method Of Noninvasive Detection And Assessment Of Gas Emboli And DCS

5a. CONTRACT NUMBER
5b. GRANT NUMBER
5c. PROGRAM ELEMENT NUMBER

6. AUTHOR(S)

5d. PROJECT NUMBER
5e. TASK NUMBER
5f. WORK UNIT NUMBER

7. PERFORMING ORGANIZATION NAME(S) AND ADDRESS(ES)
Department of Biomedical Engineering, University of Houston

8. PERFORMING ORGANIZATION REPORT NUMBER

9. SPONSORING/MONITORING AGENCY NAME(S) AND ADDRESS(ES)

10. SPONSOR/MONITOR'S ACRONYM(S)
11. SPONSOR/MONITOR'S REPORT NUMBER(S)

12. DISTRIBUTION/AVAILABILITY STATEMENT
Approved for public release, distribution unlimited

13. SUPPLEMENTARY NOTES
The original document contains color images.

14. ABSTRACT

Noninvasive functional imaging, monitoring and quantification of microbubbles forming in blood and tissues upon rapid changes in barometric pressure are extremely important for effective therapy and diagnostics of several diseases as well as for imaging and drug delivery projects. However, current techniques are unable of imaging and efficient detection of bubbles with diameter less than 50 micrometers. The goal of this proposal was to develop novel Phase- Sensitive Swept Source Optical Coherence Tomography (PhS-SSOCT) technique capable of real-time, sensitive, accurate, and noninvasive imaging, monitoring, and quantification of microbubbles in tissues. During these studies, a novel phase resolved system based on Swept Source Optical Coherence Tomography (SSOCT) has been developed. The system has an axial resolution of 10 ìm, phase sensitivity of 0.03 radians, imaging depth of up to 6 mm in air, and in-depth scanning speed of 20 kHz for a single A-line. The performance of the sensing system was carefully evaluated in optical phantoms containing gas microbubbles with different diameter. Obtained results demonstrate that bubbles with diameter greater than 10 ìm could be detected by both structural imaging and phase response whereas bubbles with diameters less than 10 ìm could be detected by the phase response of the SSOCT with high sensitivity. The accuracy for measurement of the diameter of gas microbubbles is limited to 10 ìm in structural imaging and 0.01 ìm in phase-sensitive monitoring. Preliminary studies were also performed in animals in vivo for the rapid assessment of the circulating microbubbles. The in vivo results demonstrate capability of the developed instrument to image bubbles with diameter above 8 ìm. The results from the study indicate that the developed SSOCT system could be used to detect fast-moving microbubbles and warrant further investigation in biological tissues in vivo.

15. SUBJECT TERMS

16. SECURITY CLASSIFICATION OF:			17. LIMITATION OF ABSTRACT	18. NUMBER OF PAGES	19a. NAME OF RESPONSIBLE PERSON
a. REPORT **unclassified**	b. ABSTRACT **unclassified**	c. THIS PAGE **unclassified**	**UU**	**25**	

Standard Form 298 (Rev. 8-98)
Prescribed by ANSI Std Z39-18

Introduction

Formation of microbubbles in the human body has been extensively studied by many researches since discovery of Caisson disease by Paul Bert in 1878. In its classic and most severe form, gas emboli present catastrophically (~4% of victims) with collapse, loss of consciousness, apnea, and cardiac arrest. Formation of microbubbles inside the body could be attributed due to different physiological, physical, and intervention mechanisms. These bubbles can travel to any part of the body, accounting for many serious (and sometimes life-threatening) disorders [1]. Gas bubbles in the back or joints can cause localized pain (the bends). In the spinal cord or peripheral nerve tissues, bubbles may cause paresthesias, neurapraxia, or paralysis. A bubble forming in the circulatory system can lead to pulmonary or cerebral gas emboli. Formation and/or introduction of gas microbubbles in human blood and tissues remains a serious long-term sequel in patients undergoing cardiac valve replacement (with an annual risk of up to 4%) [2-4]; cardiopulmonary bypass and other open-heart surgeries [3-8]; high-intensity focused US therapy [9-11]; cesarean section and operative hysteroscopy [12-24]; orthopedic surgery [25, 26]; and various laser ablation and laparoscopic surgeries [27-30]. Additionally, gas embolism happens in endoscopy [31], tissue biopsy [32], neurosurgery [33], liver transplantation [34-36], during central venous line insertion and removal [37, 38], and even during intravenous antibiotic delivery at home [39]. The use of ultrasound bubble contrast media could also lead to the emboli [40, 41]. Moreover, FDA and Bristol Myers Squibb Imaging issued a new alert and important safety changes to the prescribing information for DEFINITY® (Perflutren Lipid Microsphere, a diagnostic drug used as a contrast enhancement during echocardiographic procedures) in October 2007 [40]. A new clinical study found serious cardiopulmonary problems including fatalities associated with the use of DEFINITY® microbubbles likely attributed to venous gas emboli. The maximum diameter of the DEFINITY® microbubbles is 20 μm. Thus, formation and introduction of gas microbubbles in human blood and tissues is not only a problem for the divers but also is a significant everyday clinical problem affecting thousands of patients undergoing various surgical and therapeutic procedures.

Bubbles may act as emboli and block circulation, as well as cause mechanical compression and stretching of the blood vessels and nerves [42-45]. Additionally, the blood-bubble interface acts as a foreign surface, activating the early phases of blood coagulation and the release of vasoactive substances from the cells lining the blood vessels and may trigger activation of inflammatory response and, therefore, expression of different proteins and protein patters [46-54]. This can further worsen gas emboli symptoms. However, the underlying pathophysiology is still poorly understood [55]. Currently, there is no reliable method for prediction or diagnosis of bubble-associated diseases prior to commencement of apparent clinical symptoms (e.g. severe pain in joints, pulmonary problems, disorientation and mental dullness, vomiting, skin rush, and coma). It is widely recognized that **prompt detection of microbubbles in tissues and blood is the key for successful management and treatment of persons with different forms of gas emboli** [1]. Early **noninvasive** detection of bubbles forming in tissues is required for effective treatment and prediction of severity of emboli as well as for many therapeutic and research applications utilizing bubbles as contrast or drug delivery agents.

Depending on the clinical situation, the nature of the gas emboli and the number of embolic events can vary greatly. For example, Hills and Butler [56] measured intravascular gaseous emboli ranging from 19 up to 700 μm following decompression in living dogs. Gersh detected

bubble sizes between 60 and 300 μm in both intravascular and extravascular sites. However, several studies suggested that bubbles with diameter as small as **8 μm** could cause blockage and result in the trauma and onset of the symptoms [40, 57, 58]. Therefore, in order to be effective, an imaging or sensing technique should accurately detect bubbles with diameter ≥8μm.

The number of embolic signals can also show wide variations. Georgiadis *et al.* recorded between 0 and 620 embolic events per 30 min period for patients with prosthetic heart valves [59]. Mullges *et al.* have observed between 0.53 and 59.05 embolic signals per minute during extracorporeal circulation in patients undergoing cardiac surgery [60]. However, these observations were limited by the resolution of utilized technique (that is 50 μm at the best) and actual number of "trouble" microbubbles (diameter ≥ 8 μm) remains unknown. Accordingly, development of a device that allows detection of small microbubbles with sufficient accuracy and sensitivity would be a valuable tool for embolism studies, either for clinical or pre-clinical or both.

Previously, several imaging techniques have been proposed and applied to study microbubbles in blood and tissues including Doppler Sonography, MRI, Nuclear Imaging, and Computer Tomography. Doppler Sonography, the most popular technique since air-bubble interface produce strong ultrasonic reflection in the region of 1 MHz to 20MHz, is an ultrasound diagnostic imaging technique, enhanced with Doppler effect, capable of assessment moving bubbles by calculating frequency shift of a particular sample volume [61, 62]. However, Doppler Sonography can detect only moving intravascular bubbles with a diameter of approximately 50 μm [63-65]. Evidently, the resolution of this imaging method should be improved in order to achieve sensitive imaging and assessment of small μm-sized bubbles. Also, new method has to be developed for detection of stationary bubbles in tissue that could be used for prediction or diagnosis of gas emboli [66].

Optics-based techniques have great intrinsic potential to achieve the goal of noninvasive imaging of microbubbles in epithelial tissues and blood microvessels. Confocal laser scanning microscopy (CLSM) [67], two-photon fluorescence microscopy (2P-FM) [68-72], and higher harmonic generation (HHG) microscopy [73, 74] are some examples of optical methods that have been applied in different fields of biological research. CLSM have significant axial and lateral resolutions, but it is limited to ~100 μm penetration depth due to high attenuation of visible/ultraviolet excitation light. 2P-FM has higher penetration depth due to near-infrared (NIR) excitation of fluorophores, but general needs of exogenous fluorophores make this technique not truly "noninvasive". HHG microscopy does not require application of exogenous fluorophores, but is very costly (a commercial Ti:sapphire system with just the basics goes for over $150K) and bulky [75].

Optical interferometric techniques are extremely sensitive to local changes in scattering, absorption, and refractive index of the tissues and cells. Since the average refractive indexes of blood, skin, and air are quite different (1.4, 1.55 and 1.0, respectively in NIR), an optical-based sensor will be capable of assessing formation of gas bubbles with ultra-high sensitivity and accuracy [76, 77]. Here we describe our progress in development of a novel functional biosensor, based on phase-sensitive Optical Coherence Tomography (OCT) technique, for noninvasive, accurate, and sensitive imaging, monitoring, and assessment of microbubbles in skin and skin's blood mirovessels by using both amplitude imaging and phase-resolved sensing methods.

OCT is a relatively novel non-invasive optical diagnostic technique that provides depth-resolved images of tissues with resolution up to few micrometers at depths of up to several millimeters. This technique was introduced in 1991 to perform tomographic imaging of the human eye [78]. Since then, OCT is being actively developed by several research groups mainly for clinical diagnostic applications (reviewed in [79-81]).

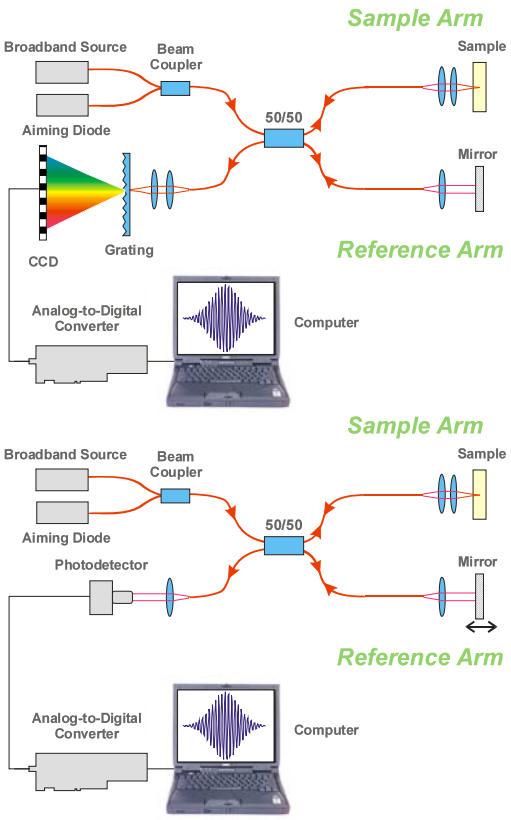

Figure 1: Schematic diagram of time domain **(**upper part**)** and spectral domain **(**lower part**)** OCT systems**.**

Current OCT-based imaging techniques may be divided into two classes: time domain OCT (TDOCT) and spectral domain OCT (SOCT) (**Figure 1**). While conventional TDOCT methods are widely used in clinical and research laboratories, recently, the significant signal-to-noise (SNR) advantage of SOCT over TDOCT (up to 30 dB) has been demonstrated [82-84]. Also, simplicity of the interferometer construction, the absence of mechanical in-depth scanning, and the SNR advantage of SDOCT are facilitating its further development for many applications. Moreover, the relaxed requirement for mechanical in-depth scanning in SOCT systems allows using a ***common*** beam path for the reference and sample arms of the interferometer with the reference plane located near the surface of the sample [85]. Such a common-path interferometer is easier to align and is less sensitive to mechanical vibrations, and it allows for more-straightforward compensation for dispersion and polarization differences between reference and sample arms.

SOCT may be further divided into two distinct methods of acquiring spectral information from an object under study: 1) Fourier-domain OCT (FDOCT) – using a broadband laser source (typical FWHM > 75 nm) with a grating and a photodiode array in the detection arm; and 2) swept-source OCT (SSOCT) - using a rapidly tunable, narrow-linewidth laser source over a broad optical bandwidth with a single photodiode in the detection arm. While FDOCT and SSOCT have similar sensitivity advantages over conventional TDOCT systems [82], the SSOCT system can detect interference fringes over a substantially longer range of time delays between reflections from reference and sample interfaces.

Phase-sensitive measurements of biological objects provide additional information on optical properties and play a key role in development of functional OCT (fOCT) methods. Recently introduced TDOCT with differential phase contrast [86, 87] shows great potential for imaging and classification of tissues as well as for fOCT [88]. While conventional OCT is based on the detection and analysis of amplitude (or spectrum) of back-scattered optical radiation, the phase sensitive OCT utilizes the phase information obtained from two tissue interfaces by the same or two probing beams. Variations in the sample refractive index will be reflected in the phase difference, $\Delta\varphi$, between these two signals from different interfaces. The phase sensitive OCT

technique (that could be both TDOCT or FDOCT) is capable of measuring Angstrom scale path length change between the beams (associated with the phase difference as $\Delta p = \frac{\lambda}{4\pi}\Delta\varphi$) in tissues [88, 89].

In OCT, a two-beam interferometer is used to detect the backscattered photons from a tissue of interest within the coherence length of the laser source. Typically, a broadband low coherence laser source is split into two arms (reference arm and sample arm). The scattered light from the sample is captured in such a way that it recombines with the light from the reference arm which results in the formation of fringes, provided the distance travelled by light in both arms does not differ by more than the coherence length of the laser source. The interference signals are recorded by the photo detector which is given by the Equation 1:

$$i(t) \propto 2\sqrt{P_r P_s}\,\cos 2k\delta(t)\ , \qquad \textbf{(1)}$$

where *i(t)* is the recorded signal from the detector and *δ(t)* is the introduced path difference . P_r, P_s are the optical powers from the reflected and the sample arms, respectively, and *k* is the wave number. The equation shows only the signal in the interferometric term neglecting zero frequency component. Rewriting equation 1 will give:

$$i(t) \propto Real\left\{\int S(\omega-\omega_0)e^{-j\Delta\emptyset(\omega-\omega_0)}\frac{d(\omega-\omega_0)}{2\pi}\right\}, \qquad \textbf{(2)}$$

where $\Delta\emptyset(\omega) = \frac{2\pi}{\lambda} * \Delta\delta\ (\omega)$ is the phase delay due to the path difference $\delta\ (\omega)$, and $S(\omega)$ is the spectrum of the source. The *i(t)* and *Δø(ω)* are Fourier Transform pairs, thus by applying a complex Fast Fourier Transform (FFT) algorithm to *i(k)*, which is *i(t)* in k-space ($k = \frac{2\pi}{\lambda}$), one can obtain a 1-D OCT depth profile. By generating transversal set of similar 1-D depth profiles with a scanning galvo-mounted mirror, a 2-D image could be constructed. Thus, 2D image contains both axial and transverse information.

For a Swept Source laser, k (t) = *2π/λ(t)* is the wave number that does not always obey a linear relation $k(t) = k_0 + k_1 t$. In theory if it obeys a linear relation, then the laser would have effectively mapped the k-space to time domain, i.e., i(t) = i(k). In reality, the frequency sweep of the chirped laser is non-linear. The *k(t)* contains higher order terms and causes non-linearity in the frequency sweep which leads to a non-uniform sampling interval. As the Fourier transform is applied to get the depth information, uniformly-spaced samples are required. By performing Non-Uniform Fourier Transformation (NUFT), depth information from the non-uniformly spaced samples can be obtained. Another approach is by using the interference fringes from a fabry-perot interferometer, uniformly spaced samples are obtained. The non-linearity in frequency sweep is analyzed by several groups and proposed different methods to overcome the problem. In this design we employs a Mach-Zehnder interferometer based optical clock (MZI-OC) which generates equally-spaced frequency interferogram that range from 12.5 GHz to 200 GHz. All peaks, as well as the zero crossings in the recorded fringes of MZI-OC, are always equally spaced in optical frequency space and are used for recalibration. The samples are collected at these zero crossings thus eliminating the non-linearity in the sampling interval. This

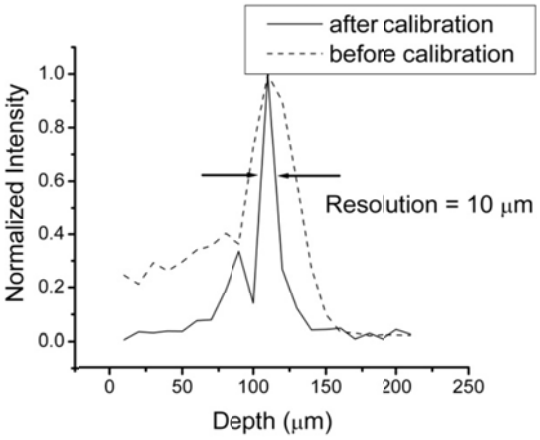

Figure 2: Improvement in resolution of SSOCT after calibration

also serves the purpose of converting into the uniform k-space. Without calibrating and remapping to uniform k-space, resolution degradation is observed along the z-space. In addition to that, this correction offered a significant improvement in the resolution at a particular depth as shown in **Figure 2**: the reflectivity profile from a weak reflector without calibrating (dotted) and with calibrating (solid) of the signal.

In this report, we present results on development of a phase resolved sensing system based on SSOCT and evaluated its performance by quantifying microbubbles of different diameters in clear and scattering tissue-simulating media and in pilot *in vivo* experiments.

Development of Phase-Sensitive Swept Source Optical Coherence Tomography System

A schematic diagram of the developed Phase-Sensitive SSOCT (PhS-SSOCT) system is shown in **Figure 3**. The system consists of four main units: the source, the interferometer (Mach-Zehnder in this particular setup), the calibration system and the data acquisition electronics. The laser source output is split into two arms: one arm containing the interferometer and the other arm containing the recalibration and triggering unit. A 90-10 fiber coupler (Thorlabs) is used to send 90% of the light to the interferometer so that the sample arm gets the maximum power. The remaining 10% is further split by a 99-1 fiber coupler with 99% going to a Fiber Bragg Grating (FBG) and 1% to the MZI-OC. The 99% light goes to the FBG through a three-arm circulator and the reflected

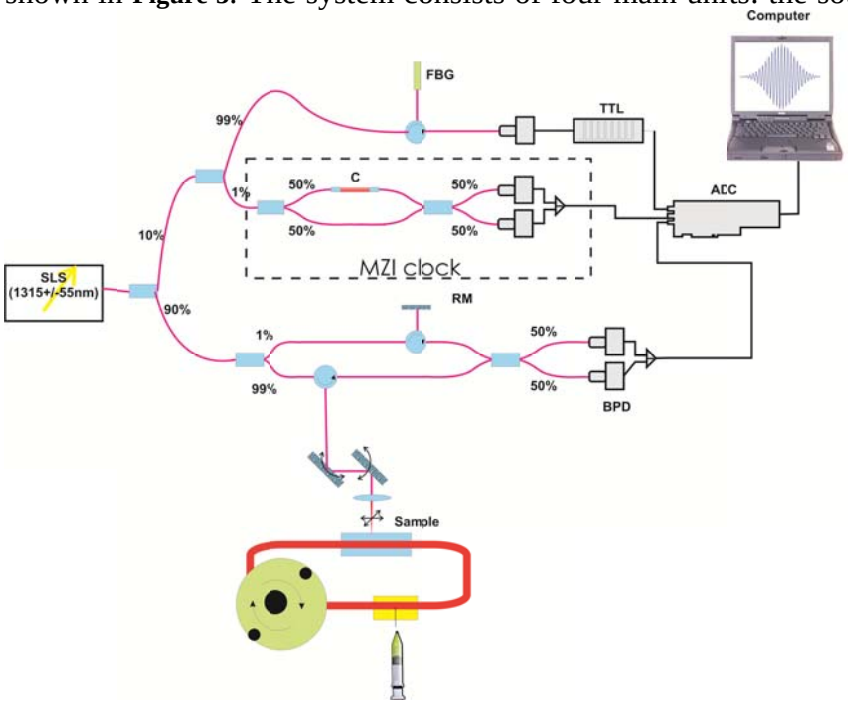

Figure 3: Basic set up of Ph-SSOCT for imaging of microbubbles (ADC: Analog to Digital Converter, BPD: Balanced Photo Detector, C: Collimators, FBG: Fiber Bragg Grating, G: Galvanometer Scanner, L: Lens, RM: Reflective Mirrors, SLS: Swept Laser Source, TTL: TTL Signal Generator).

pulse is passed to the detector by the third arm of the circulator. This detector outputs a voltage signal which is converted to an electrically tunable TTL pulse by a pulse generator (Stanford Research Systems, Inc.). The TTL signal is tuned to a required duty cycle and used to trigger the analog to digital converter (ADC). The other 1% is fed to the MZI-OC whose signal is detected in balanced detection mode, and these electric signals from the detector are acquired by one of the channels of the ADC. In the interferometer arm, the 90% light is split into 1% and 99%, each going to the reference arm and sample arm respectively via circulators. The light coming from the reference arm is passed through an adjustable pin hole to allow attenuation if required. The reflected light from the reference arm and sample arm are coupled into a 50-50 fiber coupler where they recombine and form the interference fringes. These fringes are then detected by a balanced photo detector (BPD), which subtracts the two signals to remove the common mode noise. As the fringes would be out of phase, this BPD is effectively adding the fringes but subtracting the common mode noise. After removing the common mode noise, the fringe encoded voltage is then amplified by a Transimpedance amplifier (TIA) and then RF modulated and acquired by a PC through the other channel of the ADC. Both the information from MZI and the interferometer is acquired simultaneously by the ADC with the receiving of the trigger from the FBG.

The fringes are acquired by a 14-bit high-speed digitizer (PCI 5122, National Instruments). The digitizer is operated at 50 MS/s and acquires 2500 sample points per A-scan. The sampling rate is chosen by considering the fact that the sampling interval should be smaller than the instantaneous line-width (0.1 nm); otherwise, a large sensitivity drop off along the depth scan would be observed. Out of these 2500 points, the first 200 and last 252 points are deleted so as to select the data corresponding to the laser wavelength scans. Both the raw signal and the MZI-OC signal will now have 2048 points. After recalibration using MZI-OC, the number of points is decreased due to the fact that the number of peaks and zeros are always less than the total number of points. As a matter of fact, if the nearest neighborhood algorithm is used to find the peaks, which gives 1 point out of 3 points, only one-third of the sample signal would be utilized. Thus, the number of peaks and zeros registered are around 600 indicating the presence of 600 raw data points. Using spline interpolation, three points are inserted between consecutive raw data points thus giving 2400 points. Again, the signal is windowed to have 2048 points. It must be noted that the points that are deleted from the raw signal should not contain any information from the signal. If, in the process of getting 2048 from 2400, any information containing the fringes is lost, then instead of getting 2048 points in the first deletion, more points are retained. The selection of points is made in such a way that the calibrated signal always has 2048 points without losing any fringe information. A complex FFT of this signal gives the depth profile and, due to the symmetry of FFT, each A-line corresponding depth is constructed using 1024 points. It is worth noting that inserting a lower number of points, e.g. two, might result in losing some of the higher frequency components which in turn might reduce the imaging depth of the system. Since the back-scattered light at a depth greater than the coherence length of the laser source cannot form fringes, the maximum imaging depth would not exceed the coherence length of the laser source.

Signal processing includes several steps, including reference subtraction, recalibrating and resampling to uniform k-space and image construction. The background signal is recorded at the beginning of every acquisition by blocking the sample arm. This signal contains the 1% residual light reflected from the reference arm and from the residual signal in the detectors due to

imperfect symmetry of the BPD. Subtracting the reference from the interference signal helps to increase the contrast and remove the artifacts. It removes the low-frequency components introduced by the reference or ambient light. Each depth profile is obtained from the Fourier transform of the interference fringe signal. The logarithm of the absolute value of this complex FFT is mapped to the gray scale to get an image of a single A-scan. By generating a transversal set of similar 1-D depth profiles with the scanning galvo-mounted mirror, a 2-D image is constructed. Thus, the 2-D image contains both axial and transverse information. By scanning the Y-mirror, enface imaging is achieved, thus allowing for 3-D imaging.

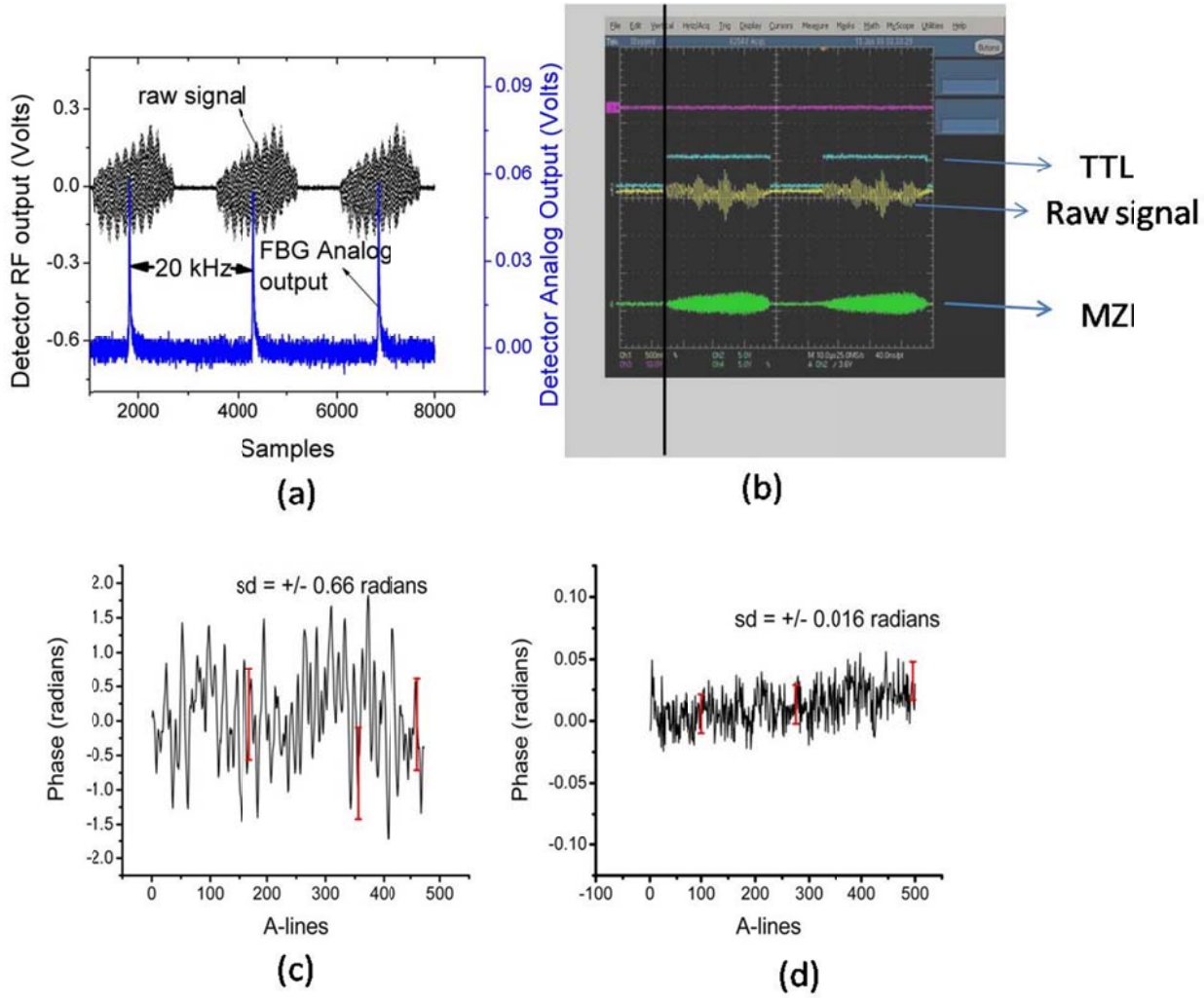

Figure 4: (a) FBG analog output and the raw signal (b) oscilloscope trace showing the synchronization of FBG trigger, raw signal and MZI-OC (c) the temporal phase response of 500 μm cuvette at 500 μm depth before stabilization and (d) after stabilization (note the scale)

Jitter present on the output source spectrum causes the acquired fringe data to slowly drift over time. These drifts introduce varying delays between the trigger signal and the subsequent digital fringe data. As the phase is extracted from the complex FFT of the fringe signal, the mismatch in fringe signal and the trigger would result in phase jumps of up to a maximum value of π as shown in **Figure 4**(a). These jumps could be removed by dynamically triggering the ADC using an electrically tunable TTL signal generated from a narrow band (0.1 nm) Fiber Bragg

Grating (FBG) as shown in **Figure 3**. A reflected optical pulse is generated whenever the source sweeps the FBG reflection wavelength. An optical pulse is detected by the detector every time the laser swept 1315 nm (the reflection wavelength of FBG), thus the frequency of the FBG pulses are also at 20 kHz as shown in **Figure 4**(a). **Figure 4**(b) depicts the oscilloscope trace showing the TTL trigger signal (2nd trace), the signal from the sample (3rd trace) and the MZI-OC signal (4th trace). This pulse is converted into a TTL signal using a signal generator (Stanford Research Systems). The TTL signal generator generates an optical pulse which can be electrically tunable to get the required duty cycle as shown in the **Figure 4**(a). By triggering the ADC with the above TTL signal, the jitter due to electronics is reduced by introducing perfect synchronization between the source and data acquisition, which in turn reduces the phase variations: standard deviation of 0.016 radians for 512 A-line scans has been achieved as shown in **Figure 4**(d).

Regardless of the above removal of π jumps, the MZI-OC introduces some phase noise to the system. This is due to the fact that zeros and peaks keep changing with every laser scan due to thermal and mechanical vibrations. Thus, the phase measured from the sampled fringe signal inhibits high phase variations. To avoid this, the MZI-OC is recorded only once and hence the zeros and peaks will not change with every scan and the recalibrated signal will be stable in the phase. The obtained uncertainty in phase is very low and is experimentally verified in the following manner. The phase shift measured in water as a function of time for different glucose concentrations and corresponding change in sample's refractive index as a function of glucose concentration are shown in **Figure 5**a and **Figure 5**b, respectively. Glucose-induced changes in

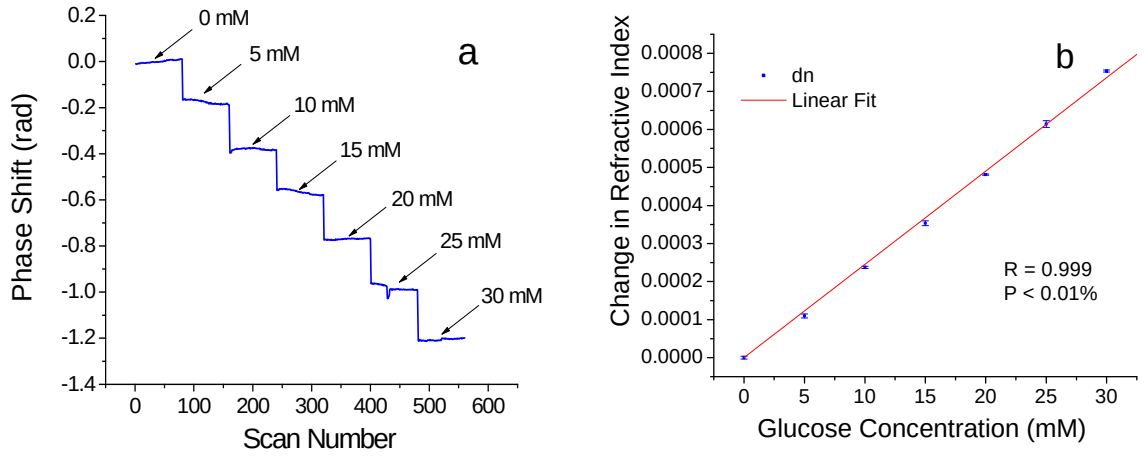

Figure 5: (a) Phase shift measured in a clear aqueous solution of glucose vs. time (or scan number); and (b) change in the sample's refractive index as a function of glucose concentration.

the refractive index, $\frac{dn}{dC}$, were calculated as $\frac{dn}{dC} = \frac{1}{d}\frac{\lambda}{4\pi}\frac{d\varphi}{dC}$, where d is the cell thickness and $\frac{d\varphi}{dC}$ is the glucose-induced changes in the phase. The standard deviation for each $\frac{dn}{dC}$ data point was calculated from 80 independent measurements of the same glucose concentration (**Figure 5**b). Linear fitting of the data points using a linear least squares algorithm yielded a correlation coefficient r>0.999 and p< 0.01%. The phase increased in equal steps indicating that the phase measured is indeed the phase introduced by the change in concentration of the glucose solution

with low uncertainty (0.03 radians). With the stabilized phase, the refractive index change as small as 6.3 x 10^{-6} (through 1 mm optical path) can be detected using the PhS-SSOCT.

Results and Discussions

Initial testing in clear media

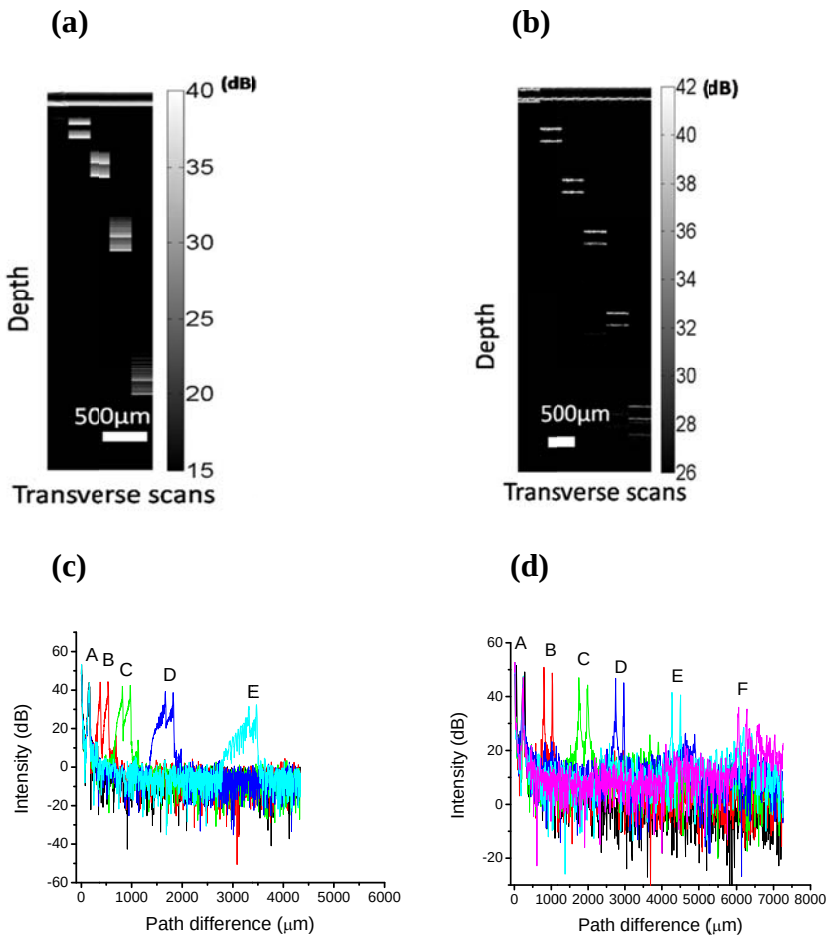

Figure 6: 2D images of a glass slide of thickness 0.16mm at different depths before (a) and after (b) recalibration and remapping to equal *k*-space and (c), (d) corresponding 1-D depth profiles. A,B,C,D,E,F are the A-line scans at different depths.

The developed system was initially characterized by using a cover glass slide (0.16 mm thick) placed in the sample arm of the interferometer. A cover glass slide is placed at five different distances from the reference arm and imaged without and with MZI-OC calibration (shown in **Figure 6**(a) and **Figure 6**(c), respectively). **Figure 6**(b) and **Figure 6**(d) show the corresponding 1D depth profiles. These data clearly demonstrate that the resolution is degraded without proper calibration and remapping into *k*-space. **Figure 6**(c) and **Figure 6**(d) shows that after proper recalibration and remapping into k-space, there was no degradation in resolution and maximum imaging depth of 6 mm is achieved.

In general, the path difference corresponding to the 3 dB drop in the 1-D profile yields the axial resolution of the system. For the developed PhS-SSOCT, an axial resolution of 10 µm and a transverse resolution of 12 µm at 20 kHz speed of an A-line scan were obtained. Theoretical axial resolution is 7 µm (computed as: $\Delta z = \frac{2(\ln 2)\lambda^2}{\pi\Delta\lambda}$). The mismatch in theoretical and measured values is attributed mainly to dispersion effects: utilized imaging lens (KBX025, Newport Corporation) disperses the ends of the wavelength scans making those wavelengths partially incoherent which effectively reduces the wavelength range and, thus, increases Δz. Transverse resolution can be enhanced by using a high numerical aperture lens with compromising the

imaging depth. However, Y. Verma et.al. recently have shown that the use of a tapered single mode fiber could increase the transverse resolution without significant decrease of the imaging depth [91].

Performance of the developed system was further evaluated in water containing gas microbubbles of different diameters. Water was injected into a 500 μm flow-through cuvette, and bubbles were generated by introducing different pressures using a peristaltic pump (Fisher Scientific). The beam is scanned across the cuvette as shown in the **Figure 7**(a). The amplitude of the interference signals in the time-delay domain was recorded from the cuvette. Four characteristic interferometric peaks were observed corresponding to the interferences between the four surfaces of the cuvette [an example is shown in **Figure 7**(b)].

In these experiments, the optical delay is calculated as a function of dynamic refractive index (modified by presence/absence of microbubbles) from the interferometric peaks that are produced by the reflection from the inner walls of the cuvette in the time-delay domain (between the surfaces 3 and 2 or B in **Figure 7**(b)). The phase is extracted from the complex Fourier transform of the interference fringes and monitored at the interferometric peak that corresponds to the self-interference between the inner glass surfaces 3 and 2. The signal from surface 2 in **Figure 7**(a) is used as a reference arm in generating the self-interference signal. Phase-sensitive measurements of water are taken before and after injection of the microbubbles. Since the bubbles induced changes in the refractive index, the diameter of the bubble from the phase shift is calculated from the Equation 3:

$$dn = \frac{1}{l}\frac{\lambda}{4\pi}\, d\varphi, \tag{3}$$

where *dn* is the refractive index change introduced by the bubble (equal to 0.33 for an air bubble in water), *l* is the diameter of the bubble, $d\varphi$ is the bubble-induced phase shift. Phase difference between the A line corresponding to the center of the bubble (determined as a maximal possible change in the phase) and the A-line outside the bubble are computed to quantify the diameters of the bubbles.

Bubbles are generated by creating a pressure difference and are circulated using the pump. Bubbles of diameters greater than 10 μm, were imaged first to test the consistency of the PhS-SSOCT imaging. The images were taken in the inter-interference mode, in which the reference

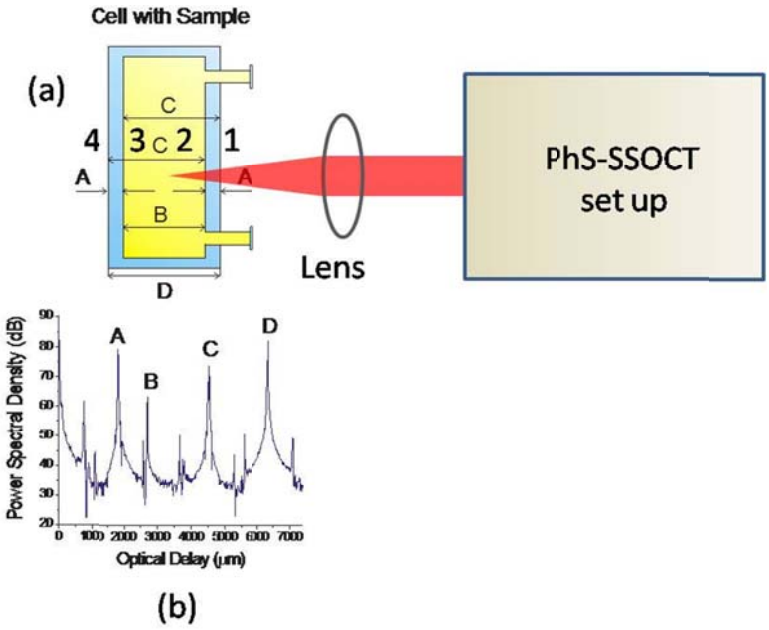

Figure 7: (a) Orientation of the cuvette with respect to the beam (b) corresponding 1-D depth profile (A- glass thickness, B- optical path thickness, C- A+B, 1,2,3,4 are the surfaces of glass cuvette).

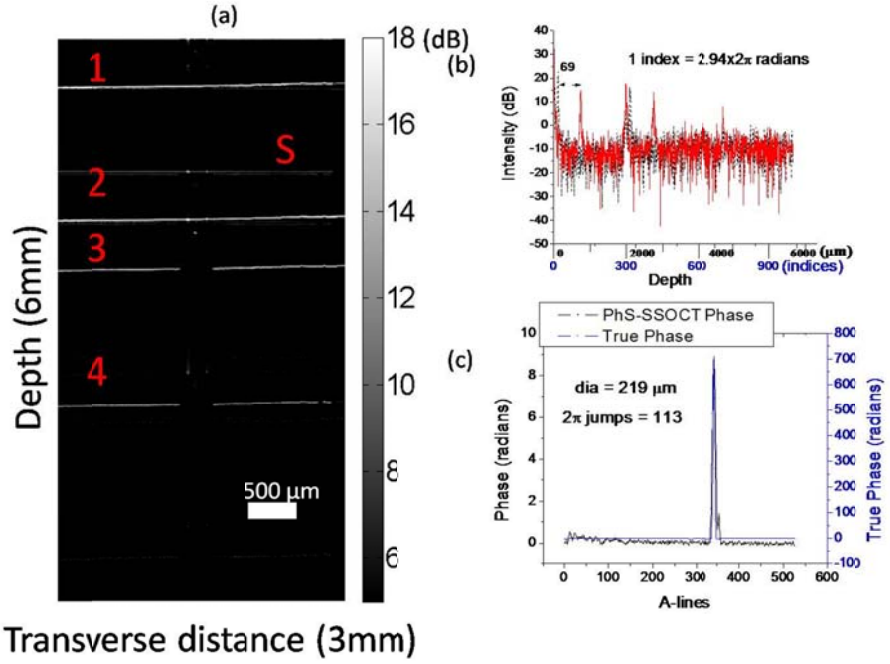

Figure 8: (a) Image of a cuvette of 500 μm thick containing a bubble of 224 μm (1,2,3,4 are the surfaces corresponding to 1,2,3,4 in figure 4(a) and S is the self-interference image) (b) corresponding 1-D profile showing the bubble induced shift in peak (c) temporal phase response at 665 μm peak.

arm can be placed in such a way that all surfaces of the cuvette (TYPE-40, NSG Precision cells, Inc.) can be shown in real distances as shown in **Figure 7**(a). Phase stability was high in self-interference mode compared to the inter-interference mode as discussed earlier. Thus, in all the results presented here, the images were taken in inter-interference mode, and the phase response was measured in self-interference mode.

Figure 8(a) shows the image of a 500 μm cuvette filled with water containing a bubble of diameter 224 μm (actual diameter). A high display threshold is selected so as to suppress the self-interference image. The 1-D profile of the corresponding self-interference image and the temporal phase response are shown in **Figure 8**(b) and **Figure 8**(c), respectively. It should be noted that the imaging and the phase response were taken one after the other in very quick succession, as the imaging was done in inter-interference mode and the phase response was studied in self-interference mode.

The reference arm is placed at a distance so that the

whole cuvette can be imaged without any negative images that arise due to the symmetry of FFT. Therefore, for **Figure 8**(a), all four bright lines correspond to all four surfaces of the cuvette. Each bright line in the **Figure 8**(a) and **Figure 9**(a), correspond to each surface of the cuvette (numbered 1 to 4 in the **Figure 7**). The missing part in the surfaces 3 and 4 is observed only in the case of huge bubbles indicating that the beam has refracted so that the reflection from the surface below the bubble is not coupled back. In the clear aqueous media, the maximal phase variations were as low as 0.03 radians after a 5-point averaging (repeated for at least 10 times), which implies that any microbubble that introduces a phase shift greater than 0.03 radians can be detected.

Generally, for an optical path difference of one wavelength the phase shift would be 2π in a homogenous media. Equation 3 describes a relationship between the changes in the refractive index and the phase of PhS-SSOCT. For an air bubble in water, the change in the refractive index would be 0.33 which translates to a minimum bubble size of 2 μm for the phase to be unwrapped by one 2π jump. Since the system's resolution is 10 μm, bubbles with diameters greater than 10 μm can be clearly seen in the structural image, as shown in **Figure 8**(a). When there is no bubble, the optical path length between the inner surfaces of the cuvette is 665 μm (refractive index of water is 1.33, so 500 μm x 1.33 = 665 μm), which is observed as a peak at 665 μm in corresponding 1-D depth profile. As the beam interacts with the bubble, the optical path length keeps decreasing until it reaches the center of the bubble and increases again to the original value. This change in the optical path length is reflected as a shift in the peak in the corresponding 1-D profile as shown in the **Figure 8**(b). The larger the bubble, the greater is the decrease in the optical path length and hence the greater is the shift. The number of 2π jumps by which the phase to be unwrapped is then calculated from the peak shifted in the 1-D profile. This unwrapped phase is then added to the PhS-SSOCT phase response to get the true phase response. For the clear media, each depth pixel corresponds to a one way physical path difference of 5.88 μm, which is equal to 2.94 "2π" jumps. Thus, for the bubble shown in **Figure 8**(a), the number of 2π jumps would be 69/2*2.94 = 113 as the peak shifts by 69 depth pixels [**Figure 8**(b)]. By plugging this true phase in Equation 3, the size of the bubble obtained is 219 μm. The actual diameter of the bubble measured is 224 μm. The true phase and the PhS-SSOCT phase (phase before adding required 2π jumps) is plotted in the same graph with two different scales on the right and left of the Y-axis.

Similarly, several bubbles with different diameters (52 μm, 94 μm, 160 μm etc.,) were taken and quantified. The obtained error ranged from 0.19 μm to 10 μm which can be attributed to the 2π ambiguity. The change in the path differences less than 10 μm is not reflected in the 1-D profile (due to limited imaging resolution of 10 μm). In this case, the number of 2π jumps by which the phase should be unwrapped cannot be determined and can take any integer value between 1 and 5. This means that microbubbles with diameters with multiples of 2 μm (up to 10 μm) would show the same phase response. For instance, if the number of 2π jumps calculated from the phase shift is 60, the actual number of 2π jumps can be any number between 60 and 65. Likewise, if the measured diameter of a bubble is 120 μm, then the actual bubble diameter could be 120, 122, 124, 126 or 128 μm. However, this ambiguity can be resolved by implementing a fast real-time continuous unwrapping algorithm which will be developed in our future studies. This algorithm would acquire multiple phase recordings between consecutive changes in the path difference of less than 2 μm and continuously unwrap the phase information. It would also allow the exact quantification of microbubbles that are beyond the imaging capabilities of the system.

Figure 9(a) show an example of small bubbles which cannot be resolved from SSOCT structural imaging. These bubbles can, however, be detected by the PhS-SSOCT. The sizes of the bubbles were estimated to be 1.9 μm (but could be 3.9 μm, 5.9 μm, 7.9 μm or 9.9 μm due to the ambiguity discussed above). Therefore, PhS-SSOCT is an effective device for ultra-sensitive

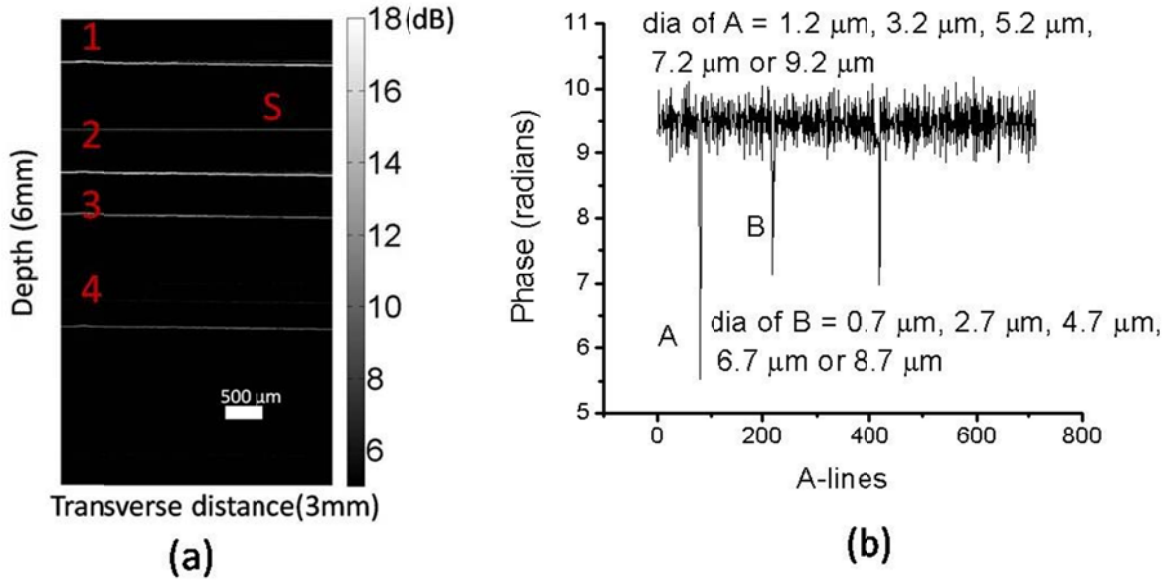

Figure 9: Image of a cuvette of 500 μm thick with (a) very small bubbles and corresponding temporal phase response at 665 μm peak (b) of (a).

quantification of microbubbles with diameters significantly less than imaging capabilities of the employed system. However, the error due to ambiguity can still be decreased by increasing the number of A-line scans with in the same frame and by reducing the focused beam diameter. For instance, as the beam propagates across the bubble, it interacts more and more of the air/gas volumes in the bubble indicating the increase in diameter. If a 10 μm bubble is scanned in 5 steps of 2 μm (the difference between two consecutive A-line diameters) each for half the bubble, then the phase would be needed to unwrap only once. Hence, no 2π ambiguities would be observed. To achieve that, a 3 mm transverse length should be scanned with 1500 A-lines as opposed to 512 A-lines. Thus, to obtain 1500 A-lines in the same time, the speed of the system should be enhanced by about 3 times, which can be achieved by using Fourier domain mode locked laser as described in [92].

Experiments with scattering tissue-simulating media

The detection, imaging and quantification of microbubbles in scattering media were also performed on a similar note. 1.54% polystyrene spheres (PS) were used to simulate the scattering media with a scattering coefficient of 100 cm^{-1} for the 1324 nm wavelength. **Figure 10**(a) depicts the image of the cuvette when filled with scattering media. A high dynamic range is chosen to identify if any self-interference lines are observed. The phase is monitored at the peak corresponding to 705 μm path length. The phase variations obtained were 0.04 radians (the same phase sensitivity is obtained even if milk is used as scattering media), indicating the minimum size of the bubble that could be detected is 0.01 μm. **Figure 10**(b) shows the image of a bubble

with an actual diameter of 142 μm, and the diameter obtained from PhS-SSOCT measurements was 143 μm from **Figure 10**(d). Note that the phase response in **Figure 10**(d) is shown for few A-lines so that the phase response could be clearly displayed.

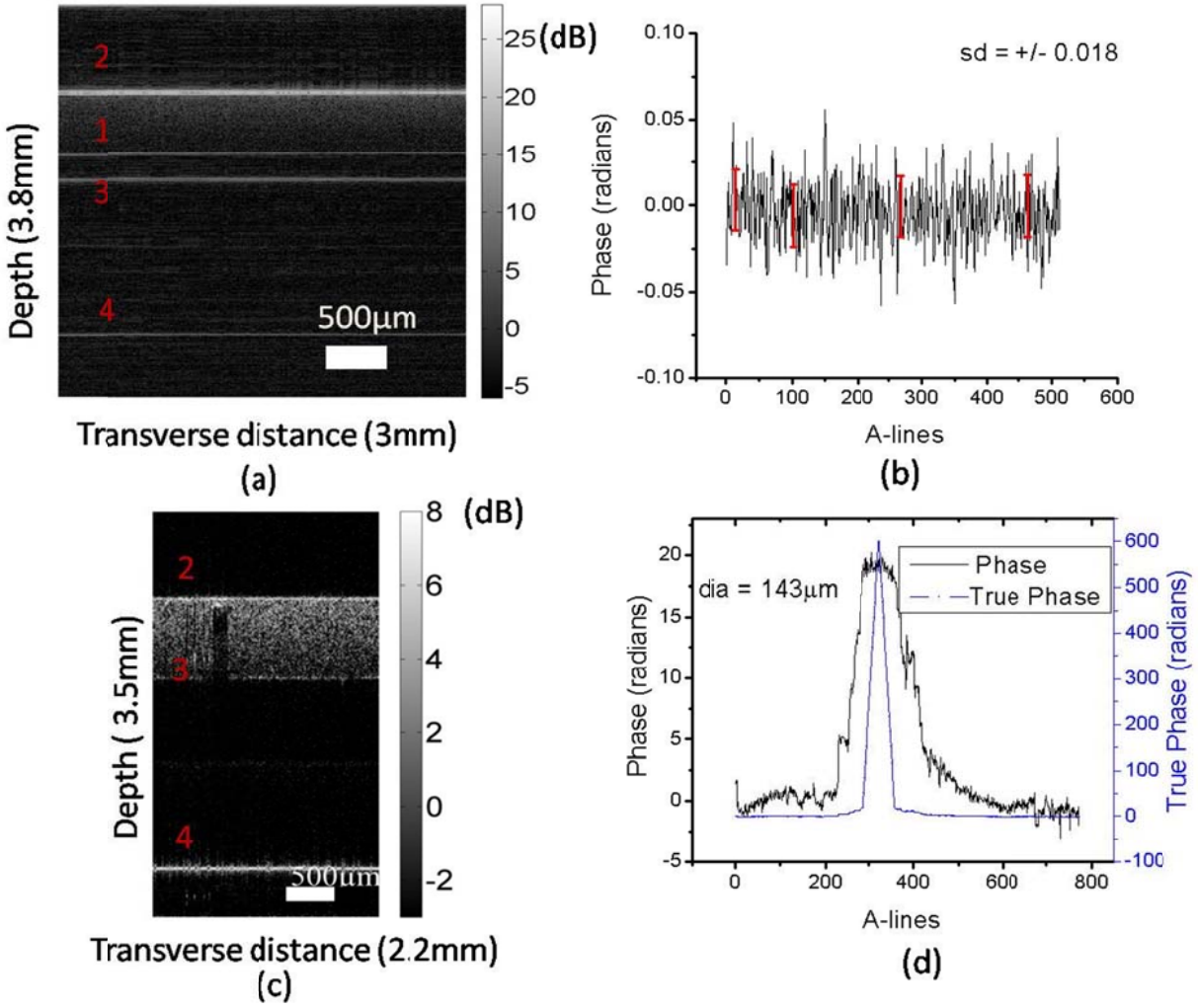

Figure 10: Image of the cuvette with scattering media (a) without any bubble (c) with a bubble and their corresponding temporal phase response at the self-interference peak in (b) and (c).

The bubbles that are beyond the imaging capabilities of SSOCT are shown in **Figure 11**. The portion circled in blue in the image is the place where the phase indicates that there could be three bubbles of diameters all around 0.8 μm (but that could be 2.8 μm, 4.8 μm, 6.8 μm or 8.8 μm). As the sizes of the bubbles are smaller than the focused beam spot (~ 25 μm), they act as a hindrance to the beam passage and create a shadow on the other interface as shown in **Figure 11**(a).

The PhS-SSOCT is also tested for detection of fast moving large bubbles. **Figure 12** depicts the M-mode image of air bubbles and air gaps that encountered the beam. The sizes of the bubbles can be predicted from the depth scan (Y-axis**)** and the speed of the bubbles from the transverse scan (X-axis). The large air gaps have a bright line at the end of the cuvette which was

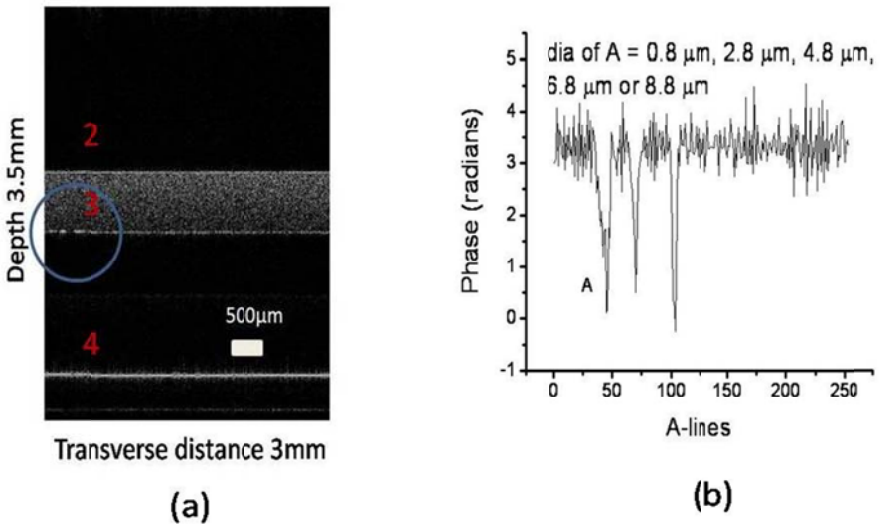

Figure 11: (a) Cuvette with very small bubbles and (b) corresponding temporal phase response.

less deep than when there was no air gap, indicating the presence of some medium that has a lower refractive index than the scattering media.

The moving bubbles could introduce a shift in phase due to the Doppler effect. The maximum phase shift that can be observed in a capillary where the maximum blood flow could be 1 mm/s, is 0.2 radians (computed using the equation 3 with β = 85 and τ = 0.15 ms).

$$v = \frac{\Delta\phi}{2n\langle k\rangle\tau cos(\beta)}, \quad \textbf{(4)}$$

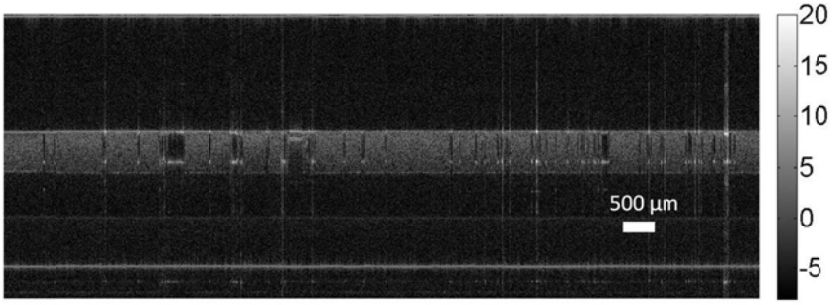

Figure 12: Image of 500 µm cuvette containing fast moving bubbles.

where V is the velocity of the bubble obtained from the Doppler image of the blood flow, k is the wave number, τ is the time taken between two A-lines and β is the angle made by the velocity vector with the laser beam. The error in quantifying the micro-bubbles that could be introduced by this phase shift from the Doppler signal could be +/- 0.06 µm. However, assuming that the bubbles and the blood flow at the same velocities, this error can be compensated by measuring the phase shift due to the Doppler effect. Our future studies include the Doppler imaging for the quantification of moving micro-bubbles in a blood flow. Further experiments would be conducted with moving bubbles to validate the compensating factor.

In Vivo Experiments

Encouraging results were obtained from preliminary *in vivo* studies with mice. Microbubbles used for these *in vivo* studies were 50% Definity microbubbles in saline and air microbubbles generated by inducing variable pressures in the syringe before injections.

Continuous imaging of the mouse tail vein at a location 2 to 3 cm upstream away from the point of injection was performed before injection, during the injection and after injection of both Definity and air microbubbles.

(a) **(b)**

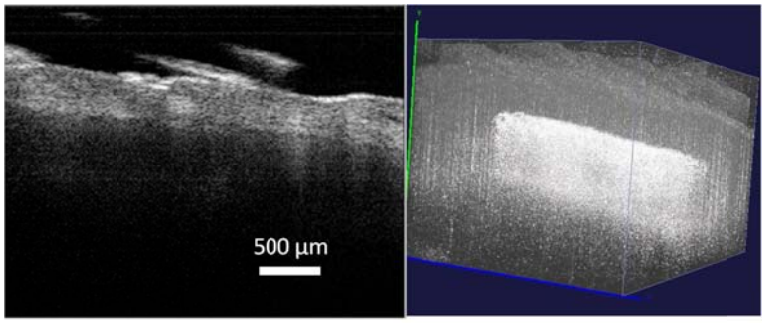

Figure 13: (a) 2D SSOCT image of a mouse tail in the blood vessel area and (b) corresponding 3D reconstruction of blood flow from Doppler signal.

Before animal experiments, we have upgraded the laser used in the system and the re-developed sensor shows now an axial resolution of 8 µm and transverse resolution of ~ 15 µm, A-line speed of 30 kHz. The 3D imaging capabilities of the system are illustrated in the **Figure 13**(a) and **Figure 13**(b). **Figure 13**(a) shows an example of a 2D image of the blood vessel in mouse tail and **Figure 13**(b) shows the 3D construction of the vessel from its corresponding Doppler signal. The 2-D images required to reconstruct the 3D were acquired at a real time speed of 40 frames per second with the frame size of 1600X500.

(a) **(b)**

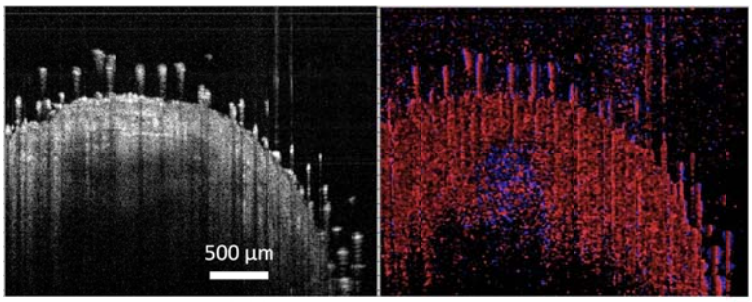

Figure 14: (a) SSOCT image of a mouse tail in the blood vessel area and (b) corresponding Doppler signal showing blood flow.

This system was then utilized for detecting Definity microbubbles injected into blood vessels of mice. Mouse tail vein was detected in both structural and the Doppler image as shown in the **Figure 14**. The vein is then continuously imaged during the injection and after injection of the Definity bubbles for 12 minutes. **Figure 15** shows the image of the vessel 9 minutes after injection of Definity. A few clusters of the Definity bubbles of sizes around 100 µm were spotted.

Similarly continuous imaging was conducted using air bubbles. **Figure 16**(a) shows an example of air microbubbles of various sizes (80 µm, 200 µm etc.,) detected by PhS-SSOCT that were induced in to the blood stream of the mouse tail vein. Similarly, a bubble of size 56 µm was spotted in the tail vein is shown in the **Figure 16**(b). Continuous imaging clearly depicts the movement of microbubbles. Hence, the developed sensor was capable of real time monitoring and quantifying of microbubbles in animals *in vivo*.

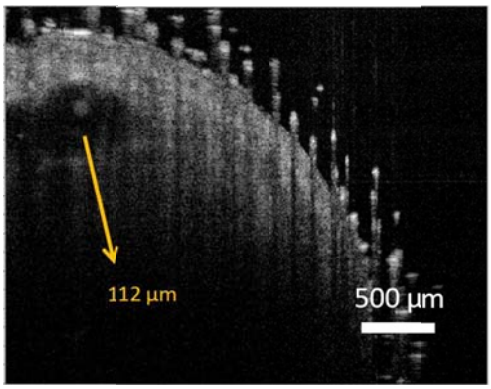

Figure 15: Cluster of Definity microbubbles spotted in real-time while circulating in the tail vein.

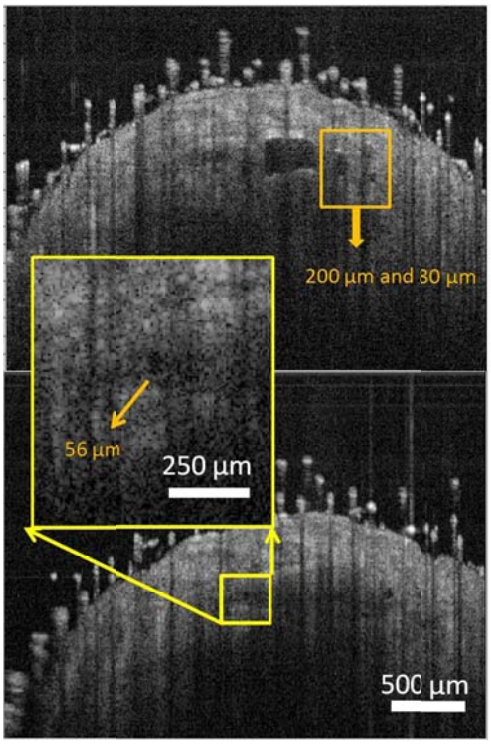

Figure 16: Air bubbles of different size spotted in the tail vein.

Conclusions

Under the sponsorship of ONR YIP, we have initiated very exciting research on development of novel class of biosensors for detection of decompression-associated illnesses. We demonstrated that the developed PhS-SSOCT is capable of imaging, detecting and quantifying of large and small microbubbles in clear and scattering media as well as in blood microvessels *in vivo*. The images shown were taken using the conventional SS-OCT and the phase results were obtained using common path SSOCT. The results suggest that small microbubbles with diameter beyond imaging capabilities of the system can be detected and quantified using the PhS-SSOCT. Potentially, microbubbles of diameters as small as 0.01 µm (that introduce a phase shift of 0.03 radians) can be detected and quantified with this method. Our future studies will focus on the development of the effective phase unwrapping algorithm that will quantify the microbubbles without any 2π ambiguities. To our knowledge, OCT was utilized for the first time to detect microbubbles in animals *in vivo*. Moreover, microbubbles of sizes ~ 50 µm were detected for the first time in animals *in vivo*. Thus, from these results it can be inferred that the SSOCT could be built into a real time useful diagnostic tool.

Publications resulted from ONR grant support

The described results were published in 2 original and 10 contributed peer-reviewed manuscripts [93-104] and one book chapter [105].

References

[1] S. A. Pulley. (2005, *Decompression Sickness*. Available: http://www.emedicine.com/emerg/topic121.htm

[2] D. G. Grosset, D. Georgiadis, A. W. Kelman, P. Cowburn, S. Stirling, K. R. Lees, A. Faichney, A. Mallinson, R. Quin, I. Bone, L. Pettigrew, E. Brodie, T. MacKay, and D. J. Wheatley, "Detection of microemboli by transcranial Doppler ultrasound," *Tex Heart Inst J*, vol. 23, pp. 289-92, 1996.

[3] T. G. Mackay, D. Georgiadis, D. G. Grosset, K. R. Lees, and D. J. Wheatley, "On the origin of cerebrovascular microemboli associated with prosthetic heart valves," *Neurol Res*, vol. 17, pp. 349-52, Oct 1995.

[4] D. Georgiadis, D. G. Grosset, A. Kelman, A. Faichney, and K. R. Lees, "Prevalence and characteristics of intracranial microemboli signals in patients with different types of prosthetic cardiac valves," *Stroke,* vol. 25, pp. 587-92, Mar 1994.
[5] M. Kurusz and B. D. Butler, "Bubbles and bypass: an update," *Perfusion-Uk,* vol. 19, pp. S49-S55, 2004.
[6] K. Yoshitani, F. de Lange, Q. Ma, H. P. Grocott, and G. B. Mackensen, "Reduction in air bubble size using perfluorocarbons during cardiopulmonary bypass in the rat," *Anesthesia and Analgesia,* vol. 103, pp. 1089-1093, Nov 2006.
[7] S. Martens, M. Dietrich, M. Doss, H. Deschka, H. Keller, and A. Moritz, "Behavior of gaseous microemboli in extracorporeal circuits: Air versus CO2," *International Journal of Artificial Organs,* vol. 29, pp. 578-582, Jun 2006.
[8] S. Goritz, H. Schelkle, J. G. Rein, and S. Urbanek, "Dynamic bubble trap can replace an arterial filter during cardiopulmonary bypass surgery," *Perfusion-Uk,* vol. 21, pp. 367-371, 2006.
[9] V. Zderic, A. Keshavarzi, M. A. Andrew, S. Vaezy, and R. W. Martin, "Attenuation of porcine tissues in vivo after high-intensity ultrasound treatment," *Ultrasound in Medicine and Biology,* vol. 30, pp. 61-66, Jan 2004.
[10] H. L. Liu, Y. Y. Chen, W. S. Chen, T. C. Shih, J. S. Chen, and W. L. Lin, "Interactions between consecutive sonications for characterizing the thermal mechanism in focused ultrasound therapy," *Ultrasound in Medicine and Biology,* vol. 32, pp. 1411-1421, Sep 2006.
[11] W. S. Chen, C. Lafon, T. J. Matula, S. Vaezy, and L. A. Crum, "Mechanisms of lesion formation in high intensity focused ultrasound therapy," *Acoustics Research Letters Online-Arlo,* vol. 4, pp. 41-46, Apr 2003.
[12] D. E. Davies, K. I. Digwood, and J. N. Hilton, "Air-Embolism During Cesarean-Section," *Medical Journal of Australia,* vol. 1, pp. 644-646, 1980.
[13] T. W. K. Lew, D. H. B. Tay, and E. Thomas, "Venous Air-Embolism During Cesarean-Section - More Common Than Previously Thought," *Anesthesia and Analgesia,* vol. 77, pp. 448-452, Sep 1993.
[14] D. Younker, V. Rodriguez, and J. Kavanagh, "Massive Air-Embolism During Cesarean-Section," *Anesthesiology,* vol. 65, pp. 77-79, Jul 1986.
[15] A. Weissman, S. Kol, and B. A. Peretz, "Gas embolism in obstetrics and gynecology - A review," *Journal of Reproductive Medicine,* vol. 41, pp. 103-111, Feb 1996.
[16] D. R. Stoloff, R. A. Isenberg, and A. I. Brill, "Venous air and gas emboli in operative hysteroscopy," *Journal of the American Association of Gynecologic Laparoscopists,* vol. 8, pp. 181-192, May 2001.
[17] D. A. Robinson and M. S. Albin, "Venous Air-Embolism and Cesarean Sections," *Anesthesiology,* vol. 66, pp. 93-94, Jan 1987.
[18] M. Nims, H. Hallonquist, and W. Camann, "Coronary arterial air embolus occurring during cesarean delivery," *Int J Obstet Anesth,* vol. 15, pp. 166-9, 2006 Apr (Epub 2006 Jan 2006.
[19] A. Nims, H. Hallonquist, and W. Camann, "Coronary arterial air embolus occurring during cesarean delivery," *International Journal of Obstetric Anesthesia,* vol. 15, pp. 166-169, Apr 2006.
[20] Y. Mushkat, D. Luxman, Z. Nachum, M. P. David, and Y. Melamed, "Gas Embolism Complicating Obstetric or Gynecologic Procedures - Case-Reports and Review of the

Literature," *European Journal of Obstetrics Gynecology and Reproductive Biology,* vol. 63, pp. 97-103, Nov 1995.

[21] R. M. Meyer, "Venous Embolism During Cesarean-Section," *Anesthesia and Analgesia,* vol. 70, pp. 668-668, Jun 1990.

[22] N. C. Matthews and G. Greer, "Embolism During Cesarean-Section," *Anaesthesia,* vol. 45, pp. 964-965, Nov 1990.

[23] M. A. Kostash and F. Mensink, "Lethal air embolism during cesarean delivery for placenta previa," *Anesthesiology,* vol. 96, pp. 753-754, Mar 2002.

[24] J. S. Handler and P. R. Bromage, "Venous Air-Embolism During Cesarean Delivery," *Regional Anesthesia,* vol. 15, pp. 170-173, Jul-Aug 1990.

[25] W. D. Liska and B. A. Poteet, "Pulmonary embolism associated with canine total hip replacement," *Veterinary Surgery,* vol. 32, pp. 178-186, Mar-Apr 2003.

[26] J. Dalsgaard, N. P. Sand, S. Felsby, P. Juelsgaard, and K. Thygesen, "R-wave changes in fatal air embolism during bone cementation," *Scand Cardiovasc J,* vol. 35, pp. 61-4, Feb 2001.

[27] R. A. Weiss and G. Munavalli, "Endovenous ablation of truncal veins," *Seminars in Cutaneous Medicine and Surgery,* vol. 24, pp. 193-199, Dec 2005.

[28] R. S. Reust, B. C. Diener, J. S. Stroup, and G. D. Haraway, "Hyperbaric treatment of arterial CO2 embolism occuring after laparoscopic surgery: A case report," *Undersea & Hyperbaric Medicine,* vol. 33, pp. 317-320, Sep-Oct 2006.

[29] T. Lifshitz, J. Levy, I. Klemperer, and S. Levinger, "Anterior chamber gas bubbles after corneal flap creation with a femtosecond laser," *Journal of Cataract and Refractive Surgery,* vol. 31, pp. 2227-2229, Nov 2005.

[30] C. Hieber, G. Ihra, S. Nachbar, A. Aloy, A. Kashanipour, and F. Coraim, "Near-fatal paradoxical gas embolism during gynecological laparoscopy," *Acta Obstet Gynecol Scand,* vol. 79, pp. 898-9, Oct 2000.

[31] N. Akhtar, W. Jafri, and T. Mozaffar, "Cerebral artery air embolism following an esophagogastroscopy: a case report," *Neurology,* vol. 56, pp. 136-7, Jan 9 2001.

[32] F. Kodama, T. Ogawa, M. Hashimoto, Y. Tanabe, Y. Suto, and T. Kato, "Fatal air embolism as a complication of CT-guided needle biopsy of the lung," *Journal of Computer Assisted Tomography,* vol. 23, pp. 949-951, Nov-Dec 1999.

[33] J. D. Tobias, J. O. Johnson, D. F. Jimenez, C. M. Barone, and D. S. McBride, Jr., "Venous air embolism during endoscopic strip craniectomy for repair of craniosynostosis in infants," *Anesthesiology,* vol. 95, pp. 340-2, Aug 2001.

[34] M. Arcari, S. D. Phillips, P. Gibbs, S. M. Rela, and N. D. Heaton, "An investigation into the risk of air embolus during veno-venous bypass in orthotopic liver transplantation," *Transplantation,* vol. 68, pp. 150-2, Jul 15 1999.

[35] G. Thiery, F. Le Corre, P. Kirstetter, A. Sauvanet, J. Belghiti, and J. Marty, "Paradoxical air embolism during orthoptic liver transplantation: diagnosis by transoesophageal echocardiography," *Eur J Anaesthesiol,* vol. 16, pp. 342-5, May 1999.

[36] R. F. Wolf, W. J. Sluiter, A. Ballast, R. Verwer, R. M. van Dam, and M. J. Slooff, "Venous air embolism, preservation/reperfusion injury, and the presence of intravascular air collection in human donor livers: a retrospective clinical study," *Transpl Int,* vol. 8, pp. 201-6, 1995.

[37] E. W. Ely, R. D. Hite, A. M. Baker, M. M. Johnson, D. L. Bowton, and E. F. Haponik, "Venous air embolism from central venous catheterization: a need for increased physician awareness," *Crit Care Med,* vol. 27, pp. 2113-7, Oct 1999.

[38] O. Vignaux, P. Borrego, L. Macron, A. Cariou, and Y. E. Claessens, "Cardiac gas embolism after central venous catheter removal," *Undersea Hyperb Med,* vol. 32, pp. 325-6, Sep-Oct 2005.

[39] T. J. Porea, J. F. Margolin, and M. M. Chintagumpala, "Radiological case of the month: pulmonary air embolus with home antibiotic infusion," *Arch Pediatr Adolesc Med,* vol. 155, pp. 963-4, Aug 2001.

[40] The US Food and Drug Administration and Bristol Myers Squibb Imaging, "IMPORTANT DRUG WARNING: Serious Cardiopulmonary Reactions," Washington, DCOctober, 12 2007.

[41] B. W. Holcomb, J. E. Loyd, B. F. Byrd, 3rd, T. T. Wilsdorf, T. Casey-Cato, W. R. Mason, and I. M. Robbins, "Iatrogenic paradoxical air embolism in pulmonary hypertension," *Chest,* vol. 119, pp. 1602-5, May 2001.

[42] A. Boussuges, F. Molenat, D. Carturan, P. Gerbeaux, and J. M. Sainty, "Venous gas embolism: Detection with pulsed Doppler guided by two-dimensional echocardiography," *Acta Anaesthesiologica Scandinavica,* vol. 43, pp. 328-332, Mar 1999.

[43] A. Boussuges, D. Carturan, P. Ambrosi, G. Habib, J. M. Sainty, and R. Luccioni, "Decompression induced venous gas emboli in sport diving: Detection with 2D echocardiography and pulsed Doppler," *International Journal Of Sports Medicine,* vol. 19, pp. 7-11, Jan 1998.

[44] B. D. Butler and W. P. Morris, "Transesophageal Echocardiographic Study Of Decompression-Induced Venous Gas Emboli," *Undersea & Hyperbaric Medicine,* vol. 22, pp. 117-128, Jun 1995.

[45] B. D. Butler, S. Luehr, and J. Katz, "Venous Gas Embolism - Time Course Of Residual Pulmonary Intravascular Bubbles," *Undersea Biomedical Research,* vol. 16, pp. 21-29, Jan 1989.

[46] D. Wallach, H. Holtmann, H. Engelmann, and Y. Nophar, "Sensitization And Desensitization To Lethal Effects Of Tumor Necrosis Factor And Il-1," *Journal Of Immunology,* vol. 140, pp. 2994-2999, May 1 1988.

[47] K. Bergh, A. Hjelde, O. J. Iversen, and A. O. Brubakk, "Variability Over Time Of Complement Activation Induced By Air Bubbles In Human And Rabbit Sera," *Journal Of Applied Physiology,* vol. 74, pp. 1811-1815, Apr 1993.

[48] A. Hjelde, K. Bergh, A. O. Brubakk, and O. J. Iversen, "Complement Activation In Divers After Repeated Air/Heliox Dives And Its Possible Relevance To Dcs," *Journal Of Applied Physiology,* vol. 78, pp. 1140-1144, Mar 1995.

[49] S. R. Kayar, E. O. Aukhert, M. J. Axley, L. D. Homer, and A. L. Harabin, "Lower decompression sickness risk in rats by intravenous injection of foreign protein," *Undersea & Hyperbaric Medicine,* vol. 24, pp. 329-335, Win 1997.

[50] A. Ersson, C. Linder, K. Ohlsson, and A. Ekholm, "Cytokine response after acute hyperbaric exposure in the rat," *Undersea & Hyperbaric Medicine,* vol. 25, pp. 217-221, Win 1998.

[51] A. Boussuges, E. Succo, I. Juhan-Vague, and J. M. Sainty, "Activation of coagulation in decompression illness," *Aviation Space And Environmental Medicine,* vol. 69, pp. 129-132, Feb 1998.
[52] I. Brenner, R. J. Shephard, and P. N. Shek, "Immune function in hyperbaric environments, diving, and decompression," *Undersea & Hyperbaric Medicine,* vol. 26, pp. 27-39, Spr 1999.
[53] C. A. Ward, D. McCullough, and W. D. Fraser, "Relation between complement activation and susceptibility to decompression sickness.," *J Appl Physiol,* vol. 62, pp. 1160-1166, 1987.
[54] A. Ersson, M. Walles, K. Ohlsson, and A. Ekholm, "Chronic hyperbaric exposure activates proinflammatory mediators in humans," *Journal Of Applied Physiology,* vol. 92, pp. 2375-2380, Jun 2002.
[55] T. S. Neuman, "Arterial Gas Embolism and Decompression Sickness," *News Physiol Sci,* vol. 17, pp. 77-81, 2002.
[56] B. A. Hills and B. D. Butler, "Size distribution of intravascular air emboli produced by decompression," *Undersea Biomed Res,* vol. 8, pp. 163-70, Sep 1981.
[57] R. S. Meltzer, P. W. Serruys, J. McGhie, N. Verbaan, and J. Roelandt, "Pulmonary wedge injections yielding left-sided echocardiographic contrast," *Br Heart J,* vol. 44, pp. 390-4, Oct 1980.
[58] A. Bouakaz and N. de Jong, "WFUMB Safety Symposium on Echo-Contrast Agents: nature and types of ultrasound contrast agents," *Ultrasound Med Biol,* vol. 33, pp. 187-96, Feb 2007.
[59] D. Georgiadis, M. Kaps, M. Siebler, M. Hill, M. Konig, J. Berg, M. Kahl, P. Zunker, B. Diehl, and E. B. Ringelstein, "Variability of Doppler microembolic signal counts in patients with prosthetic cardiac valves," *Stroke,* vol. 26, pp. 439-43, Mar 1995.
[60] W. Mullges, D. Franke, W. Reents, and J. Babin-Ebell, "Brain microembolic counts during extracorporeal circulation depend on aortic cannula position," *Ultrasound Med Biol,* vol. 27, pp. 933-6, Jul 2001.
[61] R. Y. Nishi, "Doppler and ultrasonic bubble detection," in *The Physiology and Medicine of Diving,* P. B. Bennett and D. Elliott, Eds., 4 ed London: Saunders, 1993, pp. 433–453.
[62] D. N. Walder, A. Evans, and H. V. Hempleman, "Ultrasonic monitoring of decompression," *Lancet* vol. 1, pp. 897–898, 1968.
[63] R. G. Eckenhoff, C. S. Olstad, and G. Carrod, "Human-dose response relationship for decompression and endogenous bubble formation," *J Appl Physiol* vol. 69, pp. 914–918, 1990.
[64] B. A. Hills and B. D. Butler, "Size distribution of intra-vascular emboli produced by decompression," *Undersea Biomed Res* vol. 8, pp. 163–170, 1981.
[65] M. Malconian, P. B. Rock, and J. Devine, "Operation Everest II: altitude decompression sickness during repeated altitude exposure," *Aviat Space Environ Med* vol. 58, pp. 679–682, 1987.
[66] M. A. Chappell and S. J. Payne, "A method for the automated detection of venous gas bubbles in humans using empirical mode decomposition," *Ann Biomed Eng,* vol. 33, pp. 1411-21, Oct 2005.
[67] K. Reynaud, D. Nogueira, R. Cortvrindt, R. Kurzawa, and J. Smitz, "Confocal microscopy: principles and applications to the field of reproductive biology," *Folia Histochemica Et Cytobiologica,* vol. 39, pp. 75-85, 2001.

[68] B. Cheng, D. Y. Lin, X. G. Wang, D. Y. Chen, and W. Y. Ma, "Application of two-photon excitation fluorescence imaging to real-time investigation of mouse preimplantation embryo," *Spectroscopy and Spectral Analysis,* vol. 26, pp. 193-197, Feb 2006.

[69] E. Brustein, N. Marandi, Y. Kovalchuk, P. Drapeau, and A. Konnerth, ""In vivo" monitoring of neuronal network activity in zebrafish by two-photon Ca2+ imaging," *Pflugers Archiv-European Journal of Physiology,* vol. 446, pp. 766-773, Sep 2003.

[70] J. M. Squirrell, D. L. Wokosin, J. G. White, and B. D. Bavister, "Long-term two-photon fluorescence imaging of mammalian embryos without compromising viability," *Nature Biotechnology,* vol. 17, pp. 763-767, Aug 1999.

[71] V. Daria, O. Nakamura, C. Palmes-Saloma, and S. Kawata, "Enhanced depth penetration in imaging of turbid biological samples by two-photon fluorescence microscopy," *Japanese Journal of Applied Physics Part 2-Letters,* vol. 37, pp. L959-L961, Aug 1998.

[72] R. G. Summers, D. W. Piston, K. M. Harris, and J. B. Morrill, "The orientation of first cleavage in the sea urchin embryo, Lytechinus variegatus, does not specify the axes of bilateral symmetry," *Developmental Biology,* vol. 175, pp. 177-183, Apr 1996.

[73] S. W. Chu, S. Y. Chen, T. H. Tsai, T. M. Liu, C. Y. Lin, H. J. Tsai, and C. K. Sun, "In vivo developmental biology study using noninvasive multi-harmonic generation microscopy," *Optics Express,* vol. 11, pp. 3093-3099, Nov 2003.

[74] C. K. Sun, S. W. Chu, S. Y. Chen, T. H. Tsai, T. M. Liu, C. Y. Lin, and H. J. Tsai, "Higher harmonic generation microscopy for developmental biology," *Journal of Structural Biology,* vol. 147, pp. 19-30, Jul 2004.

[75] J. Squier and M. Muller, "High resolution nonlinear microscopy: A review of sources and methods for achieving optimal imaging," *Review of Scientific Instruments,* vol. 72, pp. 2855-2867, Jul 2001.

[76] V. V. Tuchin, *Optical Clearing of Tissues and Blood* vol. PM 154: SPIE Press, 2005.

[77] V. V. Tuchin, *Tissue Optics: Light Scattering Methods and Instruments for Medical Diagnosis*. Bellingham, WA: SPIE, 2000.

[78] D. Huang, E. A. Swanson, C. P. Lin, J. S. Schuman, W. G. Stinson, W. Chang, M. R. Hee, T. Flotte, K. Gregory, C. A. Puliafito, and J. G. Fujimoto, "Optical Coherence Tomography," *Science,* vol. 254, p. 1178, 1991.

[79] A. F. Fercher, W. Drexler, C. K. Hitzenberger, and T. Lasser, "Optical coherence tomography - principles and applications," *Reports on Progress in Physics,* vol. 66, p. 239, 2003.

[80] J. M. Schmitt, "Optical coherence tomography (OCT): A review," *Ieee Journal of Selected Topics in Quantum Electronics,* vol. 5, p. 1205, 1999.

[81] P. H. Tomlins and R. K. Wang, "Theory, developments and applications of optical coherence tomography," *Journal of Physics D: Applied Physics,* vol. 38, pp. 2519-2535, 2005.

[82] M. A. Choma, M. V. Sarunic, C. H. Yang, and J. A. Izatt, "Sensitivity advantage of swept source and Fourier domain optical coherence tomography," *Optics Express,* vol. 11, p. 2183, 2003.

[83] J. F. de Boer, B. Cense, B. H. Park, M. C. Pierce, G. J. Tearney, and B. E. Bouma, "Improved signal-to-noise ratio in spectral-domain compared with time-domain optical coherence tomography," *Optics Letters,* vol. 28, p. 2067, 2003.

[84] R. Leitgeb, C. K. Hitzenberger, and A. F. Fercher, "Performance of fourier domain vs. time domain optical coherence tomography," *Optics Express,* vol. 11, p. 889, 2003.
[85] A. B. Vakhtin, D. J. Kane, W. R. Wood, and K. A. Peterson, "Common-path interferometer for frequency-domain optical coherence tomography," *Applied Optics,* vol. 42, p. 6953, 2003.
[86] D. P. Dave and T. E. Milner, "Optical low-coherence reflectometer for differential phase measurement," *Optics Letters,* vol. 25, p. 227, 2000.
[87] C. K. Hitzenberger and A. F. Fercher, "Differential phase contrast in optical coherence tomography," *Optics Letters,* vol. 24, p. 622, 1999.
[88] K. V. Larin, T. Akkin, R. O. Esenaliev, M. Motamedi, and T. E. Milner, "Phase-sensitive optical low-coherence reflectometry for the detection of analyte concentrations," *Applied Optics,* vol. 43, pp. 3408-3414, 2004.
[89] K. V. Larin, R. O. Esenaliev, E. Kim, S. Oh, M. Motamedi, and T. E. Milner, "Monitoring refractive index variations in turbid media using phase-sensitive frequency-domain OCT," *Proc. of SPIE,* vol. 5690, pp. 422-425, 2005.
[90] R. K. Manapuram, V. G. R. Manne, and K. V. Larin, "Development of Phase-Stabilized Swept-Source Optical Coherence Tomography for the Ultrasensitive Quantification of Microbubbles," *Laser Physics* vol. 18, pp. 1080-1086, 2008.
[91] Y. Verma, K. Divakar Rao, S.K. Mohanty, and P.K. Gupta, "Optical coherence tomography using a tapered single mode fiber tip," *Laser Physics Letters,* vol. 4, pp. 686-689, 2007.
[92] D. C. Adler, R. Huber, and J. G. Fujimoto, "Phase-sensitive optical coherence tomography at up to 370,000 lines per second using buffered Fourier domain mode-locked lasers," *Optics Letters,* vol. 32, p. 626, 2007.
[93] R. K. Manapuram, S. A. Baranov, V. G. R. Manne, N. Sudheendran, M. Mashiatulla, S. Aglyamov, S. Emelianov, and K. V. Larin, "Assessment of wave propagation on surfaces of crystalline lens with phase sensitive optical coherence tomography," *Laser Phys. Lett.,* vol. 8, pp. 164-167, 2011.
[94] R. K. Manapuram, V. G. R. Manne, and K. V. Larin, "Phase-sensitive swept source optical coherence tomography for imaging and quantifying of microbubbles in clear and scattering media," *Journal of Applied Physics,* vol. 105, pp. 102040-10, 2009.
[95] I. V. Larina, S. N. Ivers, S. H. Syed, M. E. Dickinson, and K. V. Larin, "Hemodynamic measurements from individual blood cells in early mammalian embryos with Doppler Swept Source OCT " *Optics Letters,* vol. 34, pp. 986-988 2009.
[96] I. V. Larina, K. Furushima, M. E. Dickinson, R. R. Behringer, and K. V. Larin, "Live imaging of rat embryos with Doppler swept-source optical coherence tomography," *Journal of Biomedical Optics,* vol. 14, pp. 050506-3, 2009.
[97] K. V. Larin, I. V. Larina, M. Liebling, and M. E. Dickinson, "Live Imaging of Early Developmental Processes in Mammalian Embryos with Optical Coherence Tomography," *Journal of Innovative Optical Health Sciences,* vol. 2, pp. 253-259, 2009.
[98] M. Ghosn, N. Sudheendran, M. Wendt, A. Glasser, V. V. Tuchin, and K. V. Larin, "Monitoring of glucose permeability in monkey skin in vivo using Optical Coherence Tomography," *Journal of Biophotonics,* vol. 3, pp. 25-33, 2010.
[99] M. Ghosn, M. Leba, A. Vijayananda, P. Rezaee, J. D. Morrisett, and K. V. Larin, "Effect of Temperature on Permeation of Low Density Lipoprotein Particles through Human Carotid Artery Tissues," *Journal of Biophotonics,* vol. 10, pp. 573-580, 2009.

[100] S. Bhat, I. V. Larina, K. V. Larin, M. E. Dickinson, and M. Liebling, "Multiple Cardiac Cycle Noise Reduction in Dynamic Optical Coherence Tomography of the Embryonic Heart and Vasculature," *Optics Letters,* vol. 34, pp. 3704-3706, 2009.
[101] R. K. Manapuram, V. G. R. Manne, and K. V. Larin, "Development of phase-stabilized swept-source OCT for ultra-sensitive quantification of microbubbles," *Laser Physics,* vol. 18, pp. 1080-1086, 2008.
[102] I. V. Larina, E. F. Carbajal, V. V. Tuchin, M. E. Dickinson, and K. V. Larin, "Enhanced OCT imaging of embryonic tissue with optical clearing," *Laser Phys. Lett.*, vol. 5, pp. 476-480, 2008.
[103] M. G. Ghosn, E. F. Carbajal, N. Befrui, V. V. Tuchin, and K. V. Larin, "Differential Permeability Rate and Percent Clearing of Glucose in Different Regions in Rabbit Sclera," *Journal of Biomedical Optics,* vol. 13, pp. 021110-1 - 021110-6, 2008.
[104] M. Ghosn, E. F. Carbajal, N. Befrui, V. V. Tuchin, and K. V. Larin, "Concentration Effect on the Diffusion of Glucose in Ocular Tissues," *Optics and Lasers in Engineering,* vol. 46, pp. 911-914, 2008.
[105] K. V. Larin, "Monitoring of Glucose Diffusion in Epithelial Tissues with Optical Coherence Tomography," in *Handbook of Optical Sensing of Glucose in Biological Fluids and Tissues*, V. V. Tuchin, Ed., ed Boca Raton: CRC Press, 2009, pp. 623-656.